Amorphous-to-crystalline transformation: how the interplay between chemistry and structure drives the multi-step nucleation of ZIF-8

A. Dok[a], S. Radhakrishnan[b,g], F. de Jong[c], O. Deschaume[d], Vinod Chandran C.[b,g], Y. de Coene[e], C. Bartic[d], M. Van der Auweraer[c], W. Thielemans[f], C. Kirschhock[g], M. A. van der Veen[h], T. Verbiest[e], E. Breynaert[b,g], S. Van Cleuvenbergen[a*]*

[a]Department of Chemistry, Molecular Imaging and Photonics, KULAK – KU Leuven, E. Sabbelaan 53, 8500 Kortrijk, Belgium
[b]NMR-Xray Platform for Convergence Research (NMRCoRe), KU Leuven, 3001 Leuven, Belgium
[c]Department of Chemistry, Molecular Imaging and Photonics, KU Leuven, Leuven Chem&Tech, Celestijnenlaan 200F, 3001 Leuven, Belgium
[d]Department of Physics and Astronomy, Soft Matter Physics and Biophysics Section, KU Leuven, Celestijnenlaan 200 D - box 2416, 3001 Leuven, Belgium
[e]Department of Chemistry, Molecular Imaging and Photonics, KU Leuven Celestijnenlaan 200D, 3001 Heverlee, Belgium
[f]Department of Chemical Engineering, Sustainable Materials Lab, KU Leuven, campus Kulak Kortrijk, Etienne Sabbelaan 53, 8500 Kortrijk, Belgium
[g]Center for Surface Chemistry and Catalysis - Characterisation and Application Team (COK-KAT), KU Leuven, 3001 Leuven, Belgium
[h]Catalysis Engineering, Department of Chemical Engineering, Delft University of Technology, 2629 Delft, The Netherlands

[*]Correspondence and requests for materials should be addressed to S.V.C. (email: Stijn.vancleuvenbergen@kuleuven.be) or E.B. (email: eric.breynaert@kuleuven.be)

Nucleation, the pivotal first step of crystallization, governs essential characteristics of crystallization products, including size distribution, morphology, and polymorphism. While understanding this process is paramount to the design of chemical, pharmaceutical and industrial production processes, major knowledge gaps remain, especially with respect to the crystallization of porous solids. Also for nanocrystalline ZIF-8, one of the most widely studied metal-organic frameworks, questions regarding the species involved in the nucleation pathway and their structural and chemical transformations remain unanswered. By combining harmonic light scattering, inherently sensitive to structural changes, with NMR spectroscopy, which reveals molecular exchanges between particles and solution, we were able to capture the crystallization mechanism of ZIF-8 in unprecedented detail. This dual approach provides concurrent structural and chemical insights, revealing key processes not previously observed in ZIF crystallization. Upon mixing small charged prenucleation clusters (PNCs) are formed, exhibiting an excess of ligands and net positive charge. We show that nucleation is initiated by aggregation of PNCs, through the release of ligands and associated protons to the liquid. This leads to the formation of charge neutral amorphous precursor particles (APPs) which incorporate neutral monomers from solution, and crystallize ZIF-8. Our work highlights chemical dynamics as a vital, yet often overlooked, dimension in the multi-stage structural evolution of MOFs. By establishing the critical role of PNCs in the nucleation of ZIF-8, new pathways open up for controlling crystallization of metal-organic frameworks through targeted chemical interactions with these species.

1. Introduction

Metal-organic frameworks (MOFs) are a class of crystalline materials that form nanoporous networks by interconnection of metal-based nodes with polydentate organic ligands. Owing to their large surface area and intrinsic structural and functional diversity, MOFs can be tuned for specific applications including gas storage, separation, and catalysis. This has led to a tireless exploration of the MOF material space, with nearly a hundred thousand structures reported so far.[1] The concept of secondary building units (SBUs) has served as a basis to guide this endeavor.[2] However, despite the success of modular chemistry in rationalizing MOF synthesis, several fundamental questions remain unresolved regarding the nucleation pathway.[3] This has led to a reliance on trial and error in MOF

discovery and optimization. In order to bridge this gap, a fundamental understanding of their crystallization process is essential. Two particular areas of debate have emerged regarding the identity and role of prenucleation species and whether amorphous intermediate phases are a part of the nucleation pathway.[3] Various nucleation models in MOF crystallization propose precursors ranging from metal complexes to larger prenucleation clusters (PNCs).[4,5,6–8,9] Moreover, the emergence and role of amorphous intermediates, remain less understood in MOF systems. This contrasts with zeolite nucleation models, where amorphous gel phases are often observed and integral to the process.[10,11] Identifying prenucleation species and intermediate phases in the nucleation and growth pathway of MOFs is critical, as these can become a natural target for obtaining rational control over MOF crystallization.[9,12] To accomplish this objective, employing experimental approaches that enable multidiagnostic *in situ* monitoring of crystallization processes is imperative. Given the intricate interplay between structure and solution chemistry in MOF crystallization, methods sensitive to both aspects offer the most comprehensive insights. However, few studies have monitored both structural and chemical dynamics concurrently, leaving critical aspects of the nucleation process unresolved. A 2018 review on *in situ* mechanistic studies of MOF crystallization illustrates this gap, as only 5 out of 238 references incorporated simultaneous chemical and structural characterization.[3]

ZIF-8, one of the most widely investigated MOFs due to its excellent gas separation abilities and high stability, exemplifies the current challenges encountered in managing crystallization processes.[13] For large-scale production of ZIF-8, fast room-temperature protocols have been developed aimed at the production of nanocrystals in a straightforward and reproducible manner. However, the upscaling of these synthesis routes is currently hampered by the incomplete knowledge of the crystallization mechanism.[14] Despite the straightforward synthesis of nanocrystalline ZIF-8 by mixing an excess of 2-methylimidazole (2-MeIm) and $Zn(NO_3)_2{\cdot}6H_2O$ in a methanolic solution,[5] understanding the initial stages of its crystallization mechanism has proved remarkably complex, as most of the crystal growth takes place within minutes.[15] Insights into the structural evolution of ZIF-8 and nucleation and growth dynamics in methanolic solution have been obtained primarily through X-ray measurements. [16–18] *In situ* synchrotron small angle X-ray scattering (SAXS) data showed the formation of a population of prenucleation clusters (PNC) with a stable size of about 2 nm almost immediately after mixing, which are consumed during particle growth. In a later study, X-ray atomic pair distribution function measurements established the disordered nature of these PNC, be it in conditions where water was added to quench the synthesis.[18] Yet it remains uncertain whether these PNCs simply serve as a monomer reservoir or actively participate in particle nucleation.[5,16,17] The initial structure of the growing particles remained an open question as well, since wide-angle X-ray scattering (WAXS) detection of the crystalline framework was slightly delayed with respect to the initial detection of particle formation via SAXS. The authors speculated this might indicate the involvement of amorphous precursor particles (APP) that subsequently transform into crystalline ZIF-8.[16] Unfortunately, the time between the onset of the SAXS and WAXS signals was too small with respect to the experimental time resolution to formulate a definitive conclusion.[16] Patterson et al. studied the rapid room-temperature synthesis in methanol by in-situ LCTEM, but were unable to observe APP, speculating that the transition from APP to ZIF-8 might occur too fast to observe directly.[19] The notion of the potential importance of APP is however strengthened by other studies in aqueous or mixed solvents, showing the presence of amorphous domains or particles coexisting within ZIF-8 crystallites.[4,13,18–23] Notably, Ogata et al. directly observed APPs through cryoTEM, subsequently transforming into ZIF-8.[24] Using aqueous environment, certain conditions even allow isolating stable amorphous particles and clusters, which are not observed in methanolic conditions.[4,13,24] Further treatment of these stable intermediates with ethanol and surfactant or proteins allowed for a precise control over the various ZIF-8 morphologies.[20,24,4]

For the crystallization of structurally related zeolites, analogous two-step nucleation mechanisms involving APP or ion-paired PNCs have also been observed.[10,11,25–27]

In addition to structural insights, chemical studies have highlighted the importance of solution-phase dynamics in ZIF-8 crystallization. The structural development of ZIF-8 cannot be separated from the chemistry occurring in the mother liquor of the crystals. In the case of ZIF-8, a series of ligation and deprotonation reactions results in a complex chemical landscape dominated by monomeric zinc complexes almost immediately after mixing.[18,28] The pathways connecting this diverse pool of dissolved species to the final crystal structure remains a matter of debate.[5,18,28,29,30] Given that initial complexes and oligomers are overstoichiometric compared to the final composition of ZIF-8, $Zn(MeIm)_2$, the nucleation and growth process involves chemical substitution, elimination and condensation reactions that significantly impact the kinetics of the different stages.[31]

While previous studies focused on either structural characterization of nucleation and growth or chemical speciation in the mother liquor, we aim to monitor both simultaneously in real time to address open questions about the role and identity of prenucleation species and intermediate phases in ZIF-8 crystallization. A two-tiered approach combining harmonic light scattering (HLS) experiments and static nuclear magnetic resonance (NMR) spectroscopy was adopted. HLS, like other nonlinear optical methods, is particularly sensitive to structure and shows promise for studying crystallization processes.[32–40] For second harmonic scattering (SHS), this structural sensitivity is illustrated most clearly by the effect of an inversion center, which results in an effective cancellation of the response within the dipole approximation. In other words, SHS detects only non-centrosymmetric structures. In an earlier study, SHS was used to monitor the non-centrosymmetric I-43m space group of ZIF-8 during crystallization.[32] However, the combination of SHS and THS to simultaneously monitor both amorphous and crystalline phases during MOF crystallization has not been reported before. To probe the potential involvement of APPs in the crystallization pathway, we introduced third harmonic scattering (THS) as an additional probe in this study. In contrast to SHS, THS can identify all symmetries, making it possible to differentiate between amorphous phases (exclusively via THS) and crystalline ZIF-8 (via both SHS and THS).[41] Through polarization measurements, additional information about (point group) symmetry can also be derived.[32,41,42] Where HLS measures the structure of the emerging solid phase, static NMR spectroscopy was employed to deliver the inverse picture by selectively probing chemical speciation in the mother liquid. Static NMR is regularly used in crystallization studies to track solvent dynamics, solute interactions, and the impact of temperature and concentration on crystallization.[43–45] In this work, static NMR spectroscopy was used to monitor the evolution of the concentration and speciation of dissolved ZIF-8 linkers and small oligomers, as well as the concentration of mobile protons. By combining both techniques, a complete picture of all events occurring in the solid and liquid fractions of the system could be obtained, capturing the different stages of ZIF-8 crystallization. This dual approach uniquely provides concurrent structural and chemical insights, allowing us to capture the different stages of ZIF-8 crystallization with unprecedented detail and conclusively establish the role of PNC and APP. We show that small positively charged PNC form neutral APP by condensation and aggregation. Subsequently APP transform into crystalline ZIF-8 by local nucleation and growth processes. As crystallization progresses and the PNC reservoir becomes depleted, the APP are consumed and the growth mechanism switches to solution-mediated growth, in line with Ostwald ripening.

3.Results

Nanoparticle formation detected by light scattering. The fast crystallization of ZIF-8 in methanol was measured in situ with a range of time-resolved scattering techniques for a molar ratio of 1:4:1000 (Zn: 2-MeIm:MeOH). Static light scattering (SLS), and HLS were conducted simultaneously using a

continuous 543 nm laser source and a pulsed laser source at 1260 nm, respectively, for the same synthesis. While dynamic light scattering (DLS) measurements were performed separately under the same conditions. The synthesis protocol is highly reproducible when starting from the same reagent and solvent batches. Between solvent batches, small variations in induction times were observed, but overall the data shows the same trends. The small observed variations are attributed to slight differences in water content (see ESI.2.8). Due to the inherent confocal effect of SHS and THS,[42] SLS probes a much larger volume than SHS and THS and, consequently it is more sensitive to multiple scattering effect (See Fig. ESI.2.6). To limit the impact of multiple scattering effects (due to particle aggregation and precipitation) on the data analysis, either through depolarization or intensity fluctuations, the analysis was focused on the first 500 seconds of the synthesis. Both DLS and SLS indicated multiple scattering only became significant after this timeframe (See ESI.1a and ESI.2.6). Immediately after mixing, a stable scattering signal was detected for SLS and SHS, but not for THS, as shown in Fig. 1a. These signals can be attributed to the molecular (hyper-)Rayleigh scattering stemming mainly from the aromatic 2-MeIm linkers and the solvent molecules. After an induction period of 52s, labeled τ_p, SLS is the first technique that detects particle growth showing a sharp increase in scattering intensity. THS and SHS register a rapid increase in signal after approximately 72 and 84 seconds. Since, as laid out in more detail below, the increase in SHS is in line with the formation of ZIF-8, the onset time at 84 seconds is labeled $\tau_{ZIF\text{-}8}$. It is noteworthy that after the steep initial increase, reminiscent of burst nucleation, the curves do not plateau in the typical sigmoidal manner expected for classical nucleation and growth. Indeed, while the process decelerates after approximately 200 seconds, all scattering signals still display a marked increase in intensity, by a factor of 2.4, 2.7, and 2.3 for SLS, SHS, and THS respectively, between 200 and 500 seconds.

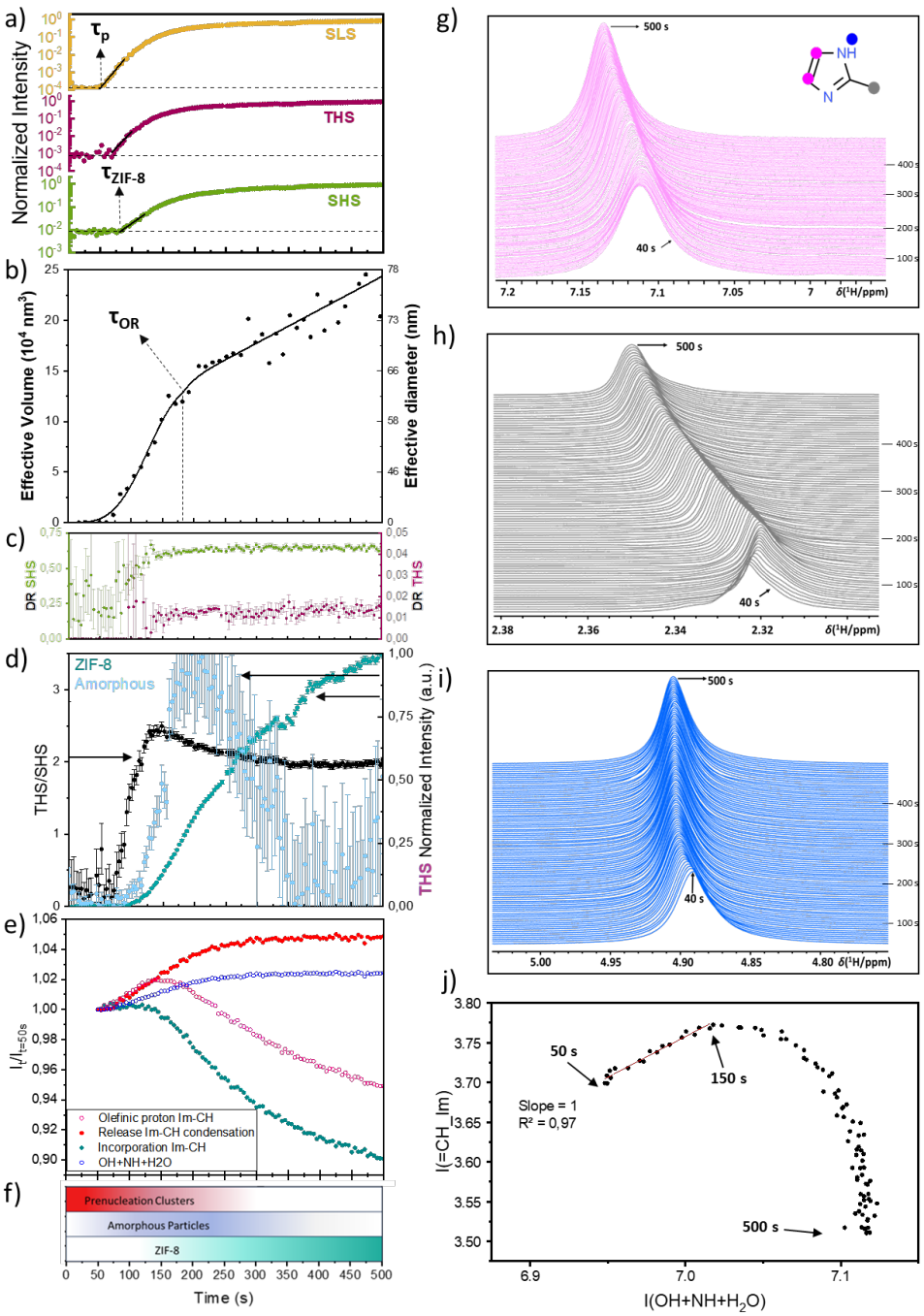


Figure 1 Time-resolved, in situ light scattering and NMR spectroscopy data collected during the crystallization of ZIF-8 from a 1:4 molar mixture of $Zn(NO_3)_2$ and 2-methylimidazole. ***a.*** *Normalized total scattering intensity (VH+VV scattering) for SLS, SHS and THS. The onset of the scattering for all harmonics was determined by intersecting a linear fit of the initial onset (black line) with the mean scattering intensity before onset (dashed line). Details are provided in ESI.2.5.* ***b.*** *Evolution of effective diameter and averaged particle volume obtained by DLS (points) and a Lifshitz and Slyozov model fit (black line) describing the data as a combination of sigmoidal Avrami growth curve, followed by Ostwald ripening.* ***c.*** *Time-resolved depolarization ratio for SHS (green) and THS (purple).* ***d.*** *Black curve: Time-evolution of the THS/SHS ratio for ZIF-8 crystal growth (left y-axis). THS and SHS signals onset around 70 and 80s respectively. Blue and green curves: THS scattering intensity evolution of the amorphous and crystalline fractions (right y-axis).* ***e.*** *Time-evolution of the integrated area of ^{1}H NMR resonances normalized to itself at T=50s, associated to the olefinic 2-methyl imidazole resonance (pink, open spheres) and , exchangeable protons corresponding to OH + NH+ H_2O (blue open spheres); The pink trace of the olefinic resonance is theoretically deconvoluted into two traces corresponding to ligand release via condensation (red closed spheres) and ligand assimilation into the ZIF-8 crystals (cyan closed spheres).* ***f.*** *Distribution of the prenucleation clusters, amorphous precursor particles and ZIF-8 particles throughout the 4 stages of the crystallization reaction.* ***g.*** *Time evolution of the ^{1}H NMR resonances of the olefinic protons of 2-methylimidazole* ***h.*** *Time evolution of the ^{1}H NMR resonance of the methyl resonance of 2-methylimidazole.* ***i.*** *Time evolution of the composite resonance of exchangeable protons (NH, OH and H_2O).* ***j.*** *Correlation plot of the absolute integrals Figure ESI.3.1) of the olefinic ^{1}H resonance of 2-methyl imidazole plotted (y-axis) and the composite resonance of exchangeable protons (x-axis). The synthesis time evolves from left to right. The red line indicates a linear fit in the timeframe between 50 and 150 s.*

Time-resolved DLS measurements, performed under identical synthesis conditions and using the finest possible time-resolution to yield a reasonable signal-to-noise ratio, allowed tracking the evolution of particle size. Figure 1b shows the evolution of the growing nanoparticles with time.

The first nanoparticles were detected around 50 seconds. At 70 seconds, a diameter around 40 nm was determined with good accuracy. Thereafter, the effective particle diameter continuously increased until a size of about 65 nm was reached at around 180 seconds. After that point, the particle size increased at a slower rate reaching 80 nm at 500 s. These results are in line with SLS measurements by Cravillon et al., who observed only minor changes in the overall size of ZIF-8 nanocrystals after 130 seconds under the same conditions.[5] The observed stages could be attributed to a nucleation and growth process followed by Ostwald ripening (OR) by fitting to a combined Johnson–Mehl–Avrami–Kolmogorov (JMAK) and Lifshitz-Slyozov model:[46]

$$V_{(t)} = \left(\left\{1 - exp\left[-\left(k_g t\right)^n\right]\right\} + (t - \tau_{OR})k_{OR}\right) V_{lim} \quad (1)$$

JMAK-LS parameters	*Fitted results*	*Description*
k_g	0.43 ± 0.047 min^{-1}	JMAK growth rate constant
n	3.5 ± 0.82	Avrami exponent
k_{OR}	0.14 ± 0.03 min^{-1}	Rate constant OR
τ_{OR}	180 ± 69 s	Onset time OR

Table 1: Fitted parameters of the JMAK-Lifshitz-Slyozov model to the measured DLS data.

The first term in equation 1 follows from the Johnson–Mehl–Avrami–Kolmogorov (JMAK) equation, with k_g a growth rate constant and n the Avrami exponent. The second term describes Ostwald ripening, with k_{OR} the rate constant and τ_{OR} the onset time of Ostwald ripening as shown in table 1. The Avrami coefficient obtained here through DLS is significantly higher than the value determined by WAXS measurements for the same synthesis.[3,47] While WAXS selectively detects the crystalline phase, DLS detects light scattering by particles, irrespective of their crystalline or amorphous nature. This mismatch may therefore point to the presence of phases without long-range periodic order. The Avrami exponent of 3.5 is in line with three dimensional growth, although the interpretation of the Avrami exponent with respect to the crystallization mechanism is generally considered problematic for solution crystallization processes.[47] Also note that the JMAK model does not specify the nucleation mechanism, which could be classical or non-classical.[46]

Unlike conventional light scattering techniques, HLS provides a measure of the symmetry of the scattering species during the crystallization process through measurement of the depolarization ratio ρ. Figure 1c shows the evolution of ρ_{SHS} and ρ_{THS}. Immediately after mixing, ρ_{SHS} has a value of ~ 0.3. This value reflects the symmetry of the 2-MeIm linkers,[32] demonstrating that these species initially dominate the SHS response. When the SHS signal starts to increase rapidly around 84 seconds at $\tau_{ZIF\text{-}8}$, ρ_{SHS} gradually shifts to a value of approximately 0.63 in line with the expected theoretical value of 2/3 for the T_d point group of ZIF-8. This confirms the formation of crystalline ZIF-8, which was further validated through ex situ powder diffraction of the final product (ESI.4.1). For THS, which is typically weaker, no measurable signal was detected prior to the onset of particle formation. ρ_{THS} assumes a value close to 0 throughout the entire process. As laid out in the materials and methods, such low values for ρ_{THS} are consistent with the formation of the highly symmetrical structure of ZIF-8 as well as APPs.

Since SHS serves as an exclusive probe for crystalline ZIF-8, while THS probes ZIF-8 as well as APPs, comparison of both responses can reveal potential contributions of an amorphous precursor. We introduce the THS to SHS ratio for this purpose. Based on equations M3 and M4 laid out in the materials and methods, THS/SHS can be reduced to:

$$\frac{THS}{SHS} \sim \frac{\sum_{zif-8,i} N_i <\left|\chi^{(3)}_{\mathrm{HRS},i}\right|^2>\langle V_i^2\rangle + \sum_{a,j} N_j <\left|\chi^{(3)}_{\mathrm{HRS,j}}\right|^2>\langle V_j^2\rangle}{\sum_{zif-8,i} N_i <\left|\chi^{(2)}_{\mathrm{HRS},i}\right|^2>\langle V_i^2\rangle} \quad (2)$$

In this equation, we omitted the negligible molecular contribution of the solvent and the solute linker molecules. Subscripts *a* and *zif-8* refer to amorphous and crystalline particles (or domains) respectively. Remark that the THS/SHS signal is proportional to the intensity of the laser source, but since the intensity remains constant during the measurement I_ω was omitted. Before discussing the results, it is instructive to consider THS/SHS within the framework of a classical nucleation process, characterized by the presence of a single crystalline species throughout the entire process. Under such circumstances, THS/SHS can be reduced to:

$$\left(\frac{THS}{SHS}\right)_{CNT} \sim \frac{N_{zif-8} <\left|\chi^{(3)}_{\mathrm{HRS},zif-8}\right|^2>\langle V^2_{zif-8}\rangle}{N_{zif-8} <\left|\chi^{(2)}_{\mathrm{HRS},zif-8}\right|^2>\langle V^2_{zif-8}\rangle} = constant \quad (3)$$

Due to the proportional increase of both the volume and number of particles, a constant value for THS/SHS is thus expected in the case of a classical nucleation scenario (CNT). Stated otherwise, deviations from a constant THS/SHS point to additional contributions from amorphous intermediates. Note that lattice defects could, in principle, contribute marginally to the THS signal by causing local deviations in the crystalline lattice. Defect formation has been reported during the early stages of ZIF-8 crystallization.[48] However, ex situ NMR measurements (ESI.4.2 NMR analysis) show no deviation from perfect stoichiometry in the final material.

For the synthesis of ZIF-8, THS/SHS is plotted in Figure 1d. It is clear that THS/SHS varies significantly over the course of the process, and hence the crystallization cannot be described according to a classical nucleation model. In the initial stage of nucleation and growth, THS/SHS increases sharply, which can only be attributed to additional contributions to the THS signal related to the formation of APPs. Even after the start of the formation of crystalline ZIF-8 at $\tau_{ZIF\text{-}8}$, THS/SHS continues to increase. This implies that the amorphous phase develops at a more rapid pace compared to the formation of crystalline ZIF-8. A plot of the growth rate for SHS and THS, calculated as the first derivative of both signals, further corroborates this (Fig. ESI.2.9). Around 150 seconds, THS/SHS reaches a maximum, after which a gradual decrease ensues. After 350 seconds, THS/SHS plateaus, as SHS and THS increase proportionally from that point onwards. In other words, after 350 seconds, the amorphous to crystalline transition is complete and SHS and THS exclusively detect the crystalline structure of ZIF-8. We can now write:

$$\left.\frac{THS}{SHS}\right|_{t>350\ s} = \frac{THS_{zif-8}}{SHS_{zif-8}} = 1.94 \quad (4)$$

Through substitution we can now express the total THS intensity as:

$$THS_{tot} = THS_a + THS_{zif-8} = THS_a + 1.94 \times SHS_{zif-8} \quad (5)$$

Since SHS_{zif-8} corresponds to the total intensity detected by SHS (SHS_{tot}), it becomes possible to separate the contributions of the amorphous and crystalline fraction throughout the process, as plotted in Figure 1d. This paints a comprehensive picture of the crystallization process. The crystallization of nanocrystalline ZIF-8 starts with the formation of APPs which amplify throughout the

initial stage. Shortly after, crystalline ZIF-8 starts forming at a slower pace. Around 180 seconds at τ_{OR}, the amorphous fraction reaches a maximum. This coincides with the switch in growth mechanism to Ostwald ripening detected by DLS (Fig. 1b). Further transformation of the APPs ensues until it is completely consumed around 350 seconds. Comparing the THS intensities for the amorphous (THS_a) and the crystalline fraction ($THS_{zif\text{-}8}$), THS_a is notably lower than THS_{zif-8} throughout the process. This might be related to the relative size of amorphous domains, as THS scales with the volume squared, and to their density, through $\boldsymbol{\chi}^{(3)}_{\mathrm{HRS},a}$.

Solution chemistry measured by static ^{1}H NMR. For the *in situ* ^{1}H NMR investigation into the formation of ZIF-8, solutions of $Zn(NO_3)_2$ and 2-methylimidazole in methanol-d_4 were prepared. Pure 2-MeIm dissolved in methanol-d_4 exhibits two distinctive ^{1}H resonances at chemical shifts of 2.3 ppm and 6.8 ppm corresponding to the methyl and olefinic protons, as depicted in Figure ESI.3.1. The FHWM of these resonances were 2.5 Hz and 2 Hz respectively. Apart from the imidazole resonances, resonances corresponding to methyl groups of residual methanol solvent at 3.3 ppm and the composite resonance of NH of imidazole and OH of methanol at 5 ppm were observed. This chemical shift to lower values in methanolic solvents is confirmed through additional experiments shown in ESI.3.3. For *in situ* static ^{1}H NMR experiments, the two solutions were mixed in a 1:4 molar ratio in a 5 mm NMR tube at time 0 s and immediately inserted in the NMR probe head, and spectra were acquired every 5 s and the results are depicted in Figures 1e-j. At 40 s, a first qualitative spectrum was acquired and from 50 s onwards, the field homogeneity and stability of the system was suitable to allow recording quantitative spectra (Figure 1g-i, Figure ESI.3.1). This is demonstrated for the trace methyl protons still present in the methanol-d4 solvent. The integral of the resonance associated with non-exchangeable methyl protons of methanol is indeed constant as shown by the red trace in Figure ESI.3.2b. This signal therefore provides an internal reference for relative quantification of all other resonances associated with dissolved species, larger than methanol (i.e. t1 $\cong$ t2; t1(species) > t1(methanol)). The use of static ^{1}H NMR implies that all observed resonances pertain exclusively to mobile protons, implying the signal exclusively reflects protons present on dissolved components and small nanoaggregates: i.e. dissolved Zn^{2+}-2-MeIm complexes, inner- or outer-sphere nanoaggregates of 2-MeIm complexes, free (unreacted) 2-MeIm, and exchangeable protons. Upon introduction of $Zn(NO_3)_2$, the olefinic resonance of 2-MeIm underwent substantial alterations, broadening to a FWHM of 40 Hz and shifting to 7.1 ppm (Figure ESI.3.1). The transition to a higher chemical shift is attributed to the complexation of Zn^{2+} ions by 2-methylimidazole. The pronounced broadening results from chemical shift broadening effects, arising from the formation of a score of Zn^{2+}-2-MeIm$^-$ and Zn^{2+}-2-MeImH complexes, and from exchange phenomena occurring between various molecular species in the solution (i.e. 2-MeImH, 2-MeImH_2^+, and 2-MeIm$^-$ incorporated in Zn^{2+}-complexes), nanoaggregates and exchangeable surface species of nanoparticles.

Detailed examination of the evolution of the resonances in the ^{1}H spectra revealed concurrent variations in the chemical shifts and integrated area (Figure 1e,j; Figures ESI.3.1-2). The non-exchangeable methyl proton resonance associated with the methanol solvent was used as internal reference for relative quantification (infra). The integrated areas corresponding to the non-exchangeable imidazole olefinic ^{1}H resonances displayed an initial increase in the timeframe between 50 and 100 s, after which the signal plateaued, before starting to gradually decline again at 150 s (Figure 1e). This initial increase is indicative of an increase in concentration of mobile (dissolved) 2-MeIm molecules. It indicates a release of 2-MeIm molecules from an immobile (solid) phase into the liquid phase. Concurrently, the area of the ^{1}H resonance associated with the exchangeable protons in the system - the NH, H_2O and OH protons (Figure 1e) - steadily increased as function of time up to around 200 s after mixing after which it plateaued. This suggests a release of exchangeable ^{1}H species

from clusters containing immobile and thus invisible 2-MeIm molecules. Linear fitting of the increase in the =CH area versus the area of the resonance associated with exchangeable protons reveals a slope of 1, hinting at release of two exchangeable protons per imidazole molecule released (Figure 1j). This is in line with particle growth by condensation via release of $MeImH_2^+$, as proposed by Yeung et al.[31] Owing to rapid protonation/deprotonation reactions, the charged $MeImH_2^+$ species quickly equilibrate with all dissolved species in solution, resulting in the overall release of dissolved linker molecules (MeImH) and protons in a ratio of 1:1. The subsequent decrease after 150 s suggests continuous assimilation of ligand into a solid phase. The 1:1 correlation between the release of exchangeable protons and linkers into solution upon condensation invites differentiation of the =CH signal into separate traces representing condensation and incorporation of neutral linkers (Figure 1e). Initially, condensation dominates linker release, but around 150 seconds, incorporation from solution becomes prevalent, with some overlap. Since the resonance from linker incorporation does not correlate with the exchangeable protons in solution, it can be inferred that the incorporated species are neutral, , e.g. MeImH or $Zn(MeIm)_2$. An initial attachment of positively charged species, with rapid release of extra linker and charge into the liquid, however, cannot be excluded.

The observed changes in the ^1H chemical shifts also provide a similar picture (Figure 1g-i). The olefinic resonance initially underwent a subtle shift to lower chemical shift, primarily up to 100 s after mixing, followed by a progressive transition to higher chemical shift (Figure 1f). The initial effect is attributed to the increased presence of free 2-MeIm molecules, indirectly indicating a depletion of Zn-ions. The transition after 100 s aligns with the crystallization of the solid fractions, indicative of intensified interactions of the 2-MeIm moieties with Zn^{2+} species and the solid constituents. The composite resonance corresponding to the OH+NH+H_2O resonances initially also showed an evolution towards higher chemical shift, consistent with the release of 2-$MeImH_2^+$(Figure 1i). Note that the resonances associated with methyl protons on 2-MeIm were explicitly excluded from the above analysis. In the context of an evolving mixed-phase system, it is important to consider the potential impact of the quantum rotor effect of methyl groups residing in nanoparticles. In static NMR, resonances associated with immobile species (i.e. species that are part of the nanoparticles) typically broaden beyond detection due to dipolar interactions. In magic angle spinning NMR (MAS NMR), this broadening is counteracted by spinning the sample at the magic angle. The quantum rotor effect of methyl groups can however have a similar effect as MAS, especially for species that are part of small nanoparticles. This can result in enhanced visibility of protons associated with methyl groups in the nanoparticles as compared to types of protons in the same particles. As this can impact the quantification of mobile versus immobile species in the system, the methyl resonance of imidazole was excluded from quantitative analysis.

Whereas light and X-ray scattering experiments exclusively detect bigger clusters and solid particles, i*n situ* static ^1H NMR spectroscopy provides information about mobile components in a system, and their evolution in time. Static ^1H NMR thus provides complementary information and assists in obtaining a comprehensive picture of the crystallization process. The ^1H NMR spectroscopy data indicates formation of oligomeric species upon mixing, which are not detectable in the static NMR spectrum. It also points towards the release of 2-MeImH and H^+ (ratio1:1) from these oligomers during the initial nanoparticle growth and suggest that the predominant imidazole species assimilated in the crystalline ZIF-8 formation phase is 2-$MeIm^-$, potentially as a complex including Zn^{2+} cations. The timescales of these findings are in alignment with those observed in the light scattering experiments. Finally, in a separate *ex situ* experiment, the quantity of linker in the solid ZIF-8 was found through quantitative NMR to closely match the expected perfect stoichiometry, indicating a defect-free final product.[49,50]

Discussion

Based on our results, we identified four key stages in the nucleation and growth mechanism of nanocrystalline ZIF-8 in methanol, which will be discussed in detail below. The onset of these stages (τ_p, $\tau_{ZIF\text{-}8}$, τ_{OR}) are indicated in Fig. 1a and 1b. Immediately after mixing, complexation leads to the formation of nanosized clusters, as detected by NMR. At τ_p (50 s), particle growth is first detected by SLS. At $\tau_{ZIF\text{-}8}$ (84 s), the appearance of crystalline ZIF-8 is confirmed through SHS measurements. Finally, at τ_{OR} (180s), the onset of Ostwald ripening is detected by a fit to the DLS data.

Prior to the detection of the first nanoparticles at τ_p, static ^{1}H NMR spectroscopy is highly sensitive to dissolved species and mobile species present in small nanoaggregates. However, as it takes some time to achieve a B^0 field homogeneity, quantitative results were only acquired from τ_p onwards. Static ^{1}H NMR measurements nevertheless indirectly provided information about the chemical species formed prior to τ_p. Contrary to expectations, the detection of the first particles coincided with an increase in the concentration of mobile imidazole in the solution (Fig. 1e). Since NMR exclusively detects species in free exchange with the solution and not those that are in the bulk of nano-particles, this implies that the imidazole molecules were initially immobilized in extended structures, and subsequently released into solution. Different studies have demonstrated that a diverse array of complexes, varying in coordination geometry and the number of coordinating imidazole molecules, forms almost immediately after mixing.[18,28,47,51] In the case of ZIF-8 synthesis in methanol, using a 1:4 metal to linker ratio, ESI-MS identified monomeric tetrahedral complexes with three methylimidazole ligands as the predominant species, aligning with similar findings in Co ZIF-67.[28] Alongside these small complexes, the formation of non-crystalline clusters preceding particle growth, a few nanometers in size, has been detected by synchrotron based experiments.[15,18,52] Since static liquid state ^{1}H NMR is able to detect ligands present in monomeric complexes but not in clusters, it follows that clusters act as the source of imidazole and proton release detected after τ_p. The continued release of linker from clusters during particle growth moreover indicates that they play a direct role in particle growth. Through correlation of the area of the olefinic imidazole resonance with that of the exchangeable protons we were able to assign the released species as 2-MeImH and H^+ in a 1:1 ratio (Figure 1j). This aligns well with a kinetic model presented by Yeung et al., who predicted that rapid equilibration of monomeric complexes leads to the formation of oligomeric prenucleation clusters, or PNCs, in a pre-equilibrium state.[47] Since these PNCs contain excess protonated ligand as compared to the final ZIF-8 stoichiometry, $Zn(MeIm)_2$, further growth involves the release of superfluous linkers and protons through condensation. The increase in concentration of mobile imidazole and protons observed by NMR after particle growth beginning at τ_p implies that particle formation results from the aggregation of PNCs rather than other possible mechanisms. If monomers from solution were attaching to PNCs, the mobile imidazole concentration would decrease as ligands become part of the solid phase. Another possible mechanism is PNC dissolution, after which released monomers would reincorporate into the growing amorphous particle precursors (APPs). However, this is incompatible with the NMR data in Fig. 1e, which show that monomer incorporation from solution (green trace) only becomes significant around 150 seconds, well after the initial APP formation. This leads to the conclusion that particle growth is primarily driven by the aggregation of PNCs. As PNCs release positive charge through condensation reactions, they neutralize gradually, promoting aggregation and resulting in the formation of APPs.

After τ_p, SLS and DLS reveal an initial exponential increase in particle size, that fits to the JMAK model (Fig. 1a and 1b). Subsequently, at $\tau_{ZIF\text{-}8}$, the crystalline phase of ZIF-8 was detected by SHS with a 35

second delay. The structural assignment of ZIF-8 was further corroborated by the SHS depolarization ratio, aligning with the I-43m space group of the crystal lattice (Fig. 1c). This observed delay in detection is reminiscent of the findings of Cravillon et al., who reported a similar lag in detection of ZIF-8's crystalline phase using synchrotron WAXS in comparison with SAXS. Since it was not clear whether this difference could be attributed to the presence of APPs, or merely to differences in sensitivity between both techniques, the authors were not able to draw definitive conclusions. In this study, SHS, akin to WAXS, demonstrated exclusive sensitivity to the crystalline form of ZIF-8, but exhibits limited sensitivity compared to SLS and DLS. Through theoretical and experimental characterization of the SHS efficiency of crystalline ZIF-8, we estimated a minimum detectable diameter of around 10 nm, which is significantly smaller than the particle size of 40 nm detected by DLS at $\tau_{ZIF\text{-}8}$ (see ESI.6). This implies that the particles detected by DLS are not entirely crystalline at this point. By incorporating THS, which, unlike SHS, is sensitive to amorphous phases, we were able to unambiguously confirm the presence of APPs. Their amorphous nature was corroborated through depolarization measurements (Fig. 1c). Through analysis of the relative progression of SHS and THS, we were moreover able to separate the evolution of the amorphous and crystalline fractions over time (Fig. 1d). Our analysis demonstrates that the formation of APPs precedes crystalline ZIF-8 formation. These APPs do not merely act as short-lived intermediates but rather drive the nucleation and growth process throughout the exponential growth stage. Growth rate analysis indeed reveals that the formation of APPs consistently outpaces that of the crystalline phase during this stage (see Figure ESI.2.9). As detailed above, NMR data indicate an increase of ligand concentration in the liquid phase upon initial formation of the APPs, consistent with PNC association, even before the appearance of crystalline ZIF-8. This implies that APPs are formed through association of PNC and subsequently transition into crystalline ZIF-8. The continuing release of linker and protons into the solution, even after the onset of crystallization, suggests that nucleation and growth of the crystalline framework occurs through condensation and particle reorganization rather than through bulk dissolution of the APPs and monomer attachment to isolated nuclei.

At τ_{OR} (180 seconds), the growth mechanism shifts from exponential growth to diffusion controlled Ostwald ripening. This shift is evidenced by a Lifshitz-Slyozov fit of the DLS data (Fig. 1b), and is marked by a reversal of the flux of mobile ligands observed by NMR (Fig. 1e), which now shows a decrease.

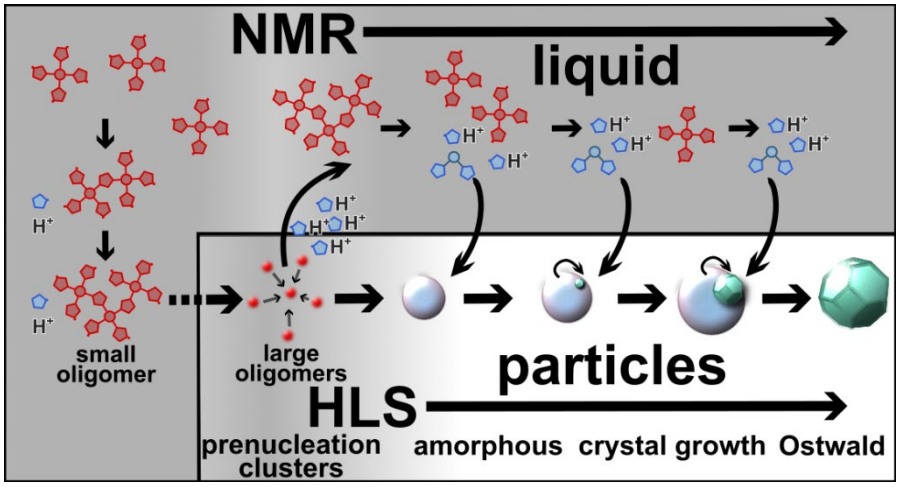


Figure 2 Scheme showing the multi-step nonclassical nucleation mechanism as derived from our observations through NMR and HLS. The key stages involved in the mechanism shown are the formation of non-crystalline PNCs through oligomerization followed by the aggregation of the PNCs into APPs by condensation. The further formation of crystalline ZIF-8 is driven by particle reorganization and condensation followed by diffusion controlled Ostwald ripening. The positively charged species are indicated in red, while neutral species are shown in blue. The crystalline framework is shown in green.

Concurrently, the rise in proton concentration registered by NMR starts to level off. This implies that further growth predominantly occurs through incorporation of monomeric species with a net stoichiometry of the product through Ostwald ripening, rather than through association-condensation. The amorphous fraction, as detected by THS (Fig. 1d), reaches a maximum at τ_{OR}, after which it starts to decrease. Synchrotron-based X-ray measurements showed a further increase in crystallinity throughout this stage,[15,53] suggesting reorganization, either intraparticle or most likely by local dissolution re-precipitation on the particle surface. Around 350 seconds, the amorphous fraction is fully depleted, while the proton concentration registered by NMR reaches a constant value. At this time, the reservoir of PNC building blocks has fully transformed into crystalline ZIF-8. Beyond this point, growth proceeds exclusively through the incremental addition of monomers.

Our observations culminate in a comprehensive mechanistic model for the nucleation and growth of ZIF-8, as summarized in Fig. 2. The different steps of the nonclassical pathway can be understood from their progression in terms of charge and stoichiometry, transitioning from positively charged, overstoichiometric species to the final stoichiometric composition, $Zn(MeIm)_2$, of the neutral charge crystalline phase. Immediately after mixing, a population of positively charged PNCs forms rapidly, containing an excess of ligands and protons compared to the final ZIF-8 structure. These PNCs release excess ligands and protons into the solution trough condensation, after which they aggregate to form APPs. These charge neutral APPs then continue to grow by incorporating neutral monomeric species from the solution. Crystallization of ZIF-8 occurs within these APPs through particle reorganization, likely involving a combination of local dissolution-reprecipitation and monomer attachment from solution. As the reservoir of PNCs depletes, the growth mechanism transitions to classical solution-mediated growth by monomer addition via Ostwald ripening. It is important to emphasize that such multistep mechanisms—incorporating both non-classical and classical mechanisms—are not unique to ZIF-8. Rather, they reflect a broader trend in complex crystallizing systems, where different mechanisms coexist or evolve through stepwise transitions.[54–56] An important aspect not directly observed in our study, but inherently present and influencing the system, involves the positively charged prenucleation species and their counter ions, notably nitrate ions (NO_3^-), which likely serve as charge compensating species. Although our methods do not detect these ions, their presence and role in balancing the positive charge of the clusters are expected to significantly impact the nucleation mechanism. A study by Priandani et al. on the modulation of $Zn(NO_3)_2$ based ZIF-8 synthesis with sodium chloride supports this notion, highlighting how varying amounts of NaCl can lead to distinct changes in crystal size and morphology, akin to those observed in solvothermal synthesis with $ZnCl_2$.[57] This opens up the exciting possibility of rational crystallization control through interaction with intermediate species in the nucleation pathway.

Conclusion

In conclusion, we were able to address two key open questions about the role of PNCs and APPs in the ZIF-8 pathway. Our results are in line with a three-step nucleation mechanism, in which positively charged PNCs form rapidly after mixing, releasing excess ligands and protons into the solution before aggregating into neutral APPs. These APPs then grow by incorporating neutral monomers and eventually crystallize into ZIF-8. Where previous studies typically focused on either structural or chemical characterization in isolation, our findings show that integrating both aspects is essential to uncover the complex mechanisms driving MOF crystallization. Without combining HLS and NMR spectroscopy, the distinct role of PNCs in the formation of APPs could not have been conclusively determined. Importantly, our approach not only deepens the understanding of the crystalline phase formation of ZIF-8 but also provides handles for controlling crystallization in MOFs through the manipulation of precursor pathways, for instance via targeted chemical interactions with PNCs through addition of counter-ions. By demonstrating the effectiveness of combining HLS and NMR spectroscopy,

we open new avenues for in-lab, real-time studies of crystallization processes. The ability of HLS to differentiate amorphous and crystalline phases, alongside its sensitivity to symmetry changes, underscores its potential as a versatile tool for studying multistep nucleation processes across diverse systems. Given the availability of ultrafast laser systems in many university laboratories and the widespread use of NMR spectrometers, this methodology offers a practical and accessible option for studying nucleation and growth mechanisms. We are convinced that our approach holds potential to offer distinctive insights into the complex nucleation and growth mechanisms of related materials, encompassing MOFs, zeolites, covalent organic frameworks and myriad other materials. Also for proteins, where amorphous liquid-like precursors often precede supramolecular order, our approach is highly promising to disentangle the underlying mechanisms of crystallization and aggregation.

6. Materials and methods

Materials

Zinc nitrate hexahydrate (98%, extra pure) was purchased from Acros Organics. 2-methylimidazole (99%) and Methanol (ACS spectrophotometric grade, >99.9%) were purchased from Sigma-Aldrich. Methanol was further purified through disposable syringe filters (Chromafil®, Glass fiber + Polyester filter, 0.20 µm pore size) purchased through Macherey-Nagel. The measurement cuvettes (High Precision Cell (QS), Light path 10x10mm) used for the *in situ* measurements were purchased through HellmaAnalytics.

Methanolic ZIF-8 synthesis was performed according to a published procedure.[5,15,58] While ZIF-8 was synthesized both *in situ* and *ex situ*, the procedure was similar. Two stock solutions were prepared, one containing the zinc source ($Zn(NO_3)_2.6H_2O$) and another containing 2-methylimidazole ($C_4H_6N_2$), with concentrations of 14.7 g/L and 16.23 g/L respectively. The two solutions were mixed to start crystallization. A 1:1 volume ratio was used to mix the stock solutions in order to reach the desired molar ratio in the form of 1:4:1000 for Zn:2-methylimidazole: methanol. For the *ex situ* synthesis the solution mixture was stirred for 24 hours at room temperature to allow nucleation and growth of the crystals. Afterwards, the crystals were separated from the reaction mixture by centrifugation and washed with methanol. This procedure was repeated 3 times followed by drying up under vacuum at 50°C for 24 hours. The *in situ* synthesis followed a similar procedure, however an automated syringe system was used to mix the two stock solutions with a 1:1 volume ratio and inject the mixture into the quartz measurement cell with a volume of 3 mL. The start of the mixing and subsequent injection into the measurement cell was used as the starting time of the reaction, but it took 5 seconds to complete injection and fill the measurement cell.

HRS theory

SHS is a nonlinear optical process in which two photons of frequency ω interact simultaneously with a material to create a new photon at double the frequency 2ω. Analogously, for THS, a three photon interaction results in a photon at triple frequency 3ω. To overcome the low probability of both processes, SHS and THS typically require illumination with pulsed laser light of much higher intensity when compared to classical (linear) light scattering.

For nanoparticles that are small compared to the wavelength of the incident light, as is the case in this study (see ESI.1a), hyper-Rayleigh scattering ensues. In this regime scattering is isotropic, meaning that the light intensity is identical for all scattering angles in the case of vertically polarized incident light. The total scattering intensity is then found as the incoherent sum over all particles:

$$I_{\mathrm{SHS}} \sim N < \left|\boldsymbol{\chi}^{(2)}_{HRS}\right|^2 > \langle V^2 \rangle \, I_\omega^2 \quad \text{(M1)}$$

$$I_{\mathrm{THS}} \sim N < \left|\boldsymbol{\chi}^{(3)}_{HRS}\right|^2 > \langle V^2 \rangle \, I_\omega^3 \quad \text{(M2)}$$

I_{SHS} and I_{THS} are linearly related to the particle concentration N and quadratically to the orientationally averaged second and third susceptibility. I_ω is the incident light intensity. Within the electric dipole approximation, SHS is forbidden for structures with inversion symmetry, as the second susceptibility $\chi^{(2)} = 0$ in this case. In contrast to SHS, there are no symmetry restrictions for THS. For a single particle the intensity of both processes scales with the particle volume (V) squared. For a collection of particles with a distribution of sizes, the intensity is therefore related to the average of the volume squared.

The scattering intensities for second- and third order processes are additive. As a result, all solution species will in principle contribute to the measured scattering intensity. Equations 3 and 4 describe the total SHS and THS intensity found for a generalized crystallization process:

$$\mathrm{I_{SHS}} \sim (\textstyle\sum_m N_m < \left|\boldsymbol{\beta}^{\square}_{\mathrm{HRS,m}}\right|^2 > + \sum_{ncs,i} N_i < \left|\boldsymbol{\chi}^{(2)}_{\mathrm{HRS},i}\right|^2 > \langle \mathrm{V}_i^2 \rangle) \mathrm{I}_\omega^2 \quad \text{(M3)}$$

$$\mathrm{I_{THS}} \sim (\textstyle\sum_n N_n < \left|\boldsymbol{\gamma}^{\square}_{\mathrm{HRS,n}}\right|^2 > + \sum_{ncs,i} N_i < \left|\boldsymbol{\chi}^{(3)}_{\mathrm{HRS},i}\right|^2 > \langle \mathrm{V}_i^2 \rangle + \sum_{cs,j} N_j < \left|\boldsymbol{\chi}^{(3)}_{\mathrm{HRS,j}}\right|^2 > \langle \mathrm{V}_j^2 \rangle) \mathrm{I}_\omega^3 \quad \text{(M4)}$$

These equations encompass the response of all solution species (with $N_{m,n,i,j}$ described as number of solution species per unit volume). Molecular species (like solvent and linker) react as per **β** and **γ**, their first and second hyperpolarizabilities. Macroscopic clusters and particles respond through their macroscopic susceptibilities $\boldsymbol{\chi}^{(2)}$ and $\boldsymbol{\chi}^{(3)}$. We have distinguished centrosymmetric (cs) and non-centrosymmetric (ncs) macroscopic contributions; the former contributing exclusively to THS, while the latter affects both SHS and THS. Notably, in crystallization, the macroscopic responses ($\boldsymbol{\chi}^{(2)}$, $\boldsymbol{\chi}^{(3)}$) often overshadow molecular ones (**β**, **γ**) early in the process, due to their volume-squared dependence.

Due to the tensorial nature of the first and second hyperpolarizability for molecules, and the second and third susceptibility for particles, polarized measurements contain additional information regarding the symmetry of species. In this study, the depolarization ratio ρ, defined as the ratio between the intensity of cross-polarized and parallel-polarized SHS and THS light, is used to interrogate symmetry.[35,37,38]

$$\rho_{\mathrm{SHS}} = \frac{I_{HV}(2\omega)}{I_{VV}(2\omega)} \quad \text{(M5)}$$

$$\rho_{\mathrm{THS}} = \frac{I_{HV}(3\omega)}{I_{VV}(3\omega)} \quad \text{(M6)}$$

In these equations the first subscript refers to the polarization of the scattered light, the second to the polarization of the incident light. H stands for horizontal polarization, V for vertical polarization. The SHS depolarization ratio ranges from 1/9 for dipolar to 2/3 for octupolar species.[42] For ZIF-8, which has octupolar T_d symmetry (I-43m space group), the depolarization ratio assumes a value of 2/3. In THS, this ratio varies from 5/8 for hexadecapolar symmetry to 0 for isotropic species. For amorphous particles a depolarization ratio of exactly 0 is expected. For T_d symmetry there is no exact solution. However, an almost isotropic response, with values near 0, can generally be assumed.[42]

HRS and SLS setup

The experimental setup to perform the light scattering measurements was described elsewhere.[59] For our use, this setup was slightly modified.[40] This setup uses a femtosecond laser (Insight DS+, Spectra-Physics) with tunable wavelength ranging from 680 to 1300 nm, as a high-power light source. For the measurements, a fundamental wavelength of 1260 nm was used at a frequency of 80 MHz width pulse widths of 120 fs. The intensity variation of the incident light and the vertical polarization was accomplished by the combination of an achromatic half-wave plate and a Glan-Taylor polarizer. For the *in situ* measurements of ZIF-8, the intensity of the incident beam was kept constant at 1 W. The light is subsequently focused into a 10 x10 mm quartz cuvette containing the solution by an aspheric lens (A220TM, Thorlabs). The resulting beam waist of the focused beam is around 8 µm and a Rayleigh length of about 190 µm.

A secondary continuous wave laser at a wavelength of 543 nm was coupled into the system for static light scattering. Again, a half-wave plate and a Glan-Taylor polarizer combination was used to ensure a vertical polarization and power modulation of the incoming light. The power of this laser light was tuned to ensure that the EMCCD camera was not saturated throughout the crystallization reaction and was set at a constant power once the optimal intensity was achieved. The secondary beam was guided and aligned to ensure the same focus positions as the primary incoming beam. However, obtained focus size was different compared to the primary beam due to the absence of the confocal effect.

The scattered light was collected under 90° and subsequently collimated and focused onto the slit of a spectrograph (Bruker IS 500) attached to an EMCCD camera (Ixon 897, Andor Oxford instruments). To collect the full image of the focal point onto the slit, a rotation of the image by 90° was achieved by a set of mirrors in a periscope system. Before the spectrograph, a Wollaston prism was placed to separate the scattered light into its vertical and horizontal polarized components. Using the grating (50 l/mm, 300 blaze) in the spectrograph allowed to separate the incoming light, allowing us to measure simultaneously the depolarization ratio for SHS, THS and SLS. The temporal resolution of the in situ measurements were limited, due to the low scattering efficiency of SHS and THS. Therefore, the data acquisition times were always kept at 4s.

Dynamic light scattering measurements

The time-resolved *in situ* measurements of methanolic ZIF-8 synthesis with dynamic light scattering was performed with a NanoBrook Omni Particle size and zeta potential analyzer (Brookhaven Instruments, Holtville NY, United States; 40 mW maximum power, 640 nm nominal wavelength red diode laser, measurement angle 173°). To achieve high temporal resolution for the *in* situ measurements, the correlograms were averaged for 10 seconds. Particle Solutions software was used to extract the number distributions and intensity of the measurements.

Powder X-ray Diffraction

X-ray diffraction (XRD) patterns were obtained on a Malvern PANalytical Empyrean diffractometer, equipped with a PIXcel3D solid-state detector using a Cu anode (using Ka1 and Ka2). The powder samples were loaded onto a 48-well sample holder and X-ray diffractograms were recorded at room temperature in a transmission geometry within a 1.3 - 45° 2θ range using a step size of 0.013°.

In situ NMR measurements

In situ ^{1}H NMR measurements were performed on a Bruker 800 MHz Avance Neo spectrometer equipped with a 5mm ^{1}H/^{2}H/X BBO probehead (^{1}H Larmor frequency 801.25 MHz). Equal volumes of 2-methyl imidazole and zinc nitrate solutions in deuterated methanol (Methanol-D_4, Sigma Aldrich) were mixed in a 1:4 molar ratio in a 5 mm NMR tube (Norrel) and inserted into the probehead. ^{1}H

spectra were acquired every 5 s with an RF pulse of 18 kHz, an acquisition time of 1s and relaxation delay of 4s. The spectra were processed and integrated using Bruker Topspin 4.0.9 software.

6. Acknowledgments

C.K. acknowledges the Flemish Government for long-term Methusalem structural funding. E.B., and C.K. acknowledge joint funding by the Flemish Science Foundation (FWO; G083318N) and the Austrian Science Fund (FWF) (funder ID 10.13039/501100002428, project ZeoDirect I 3680-N34). E.B. acknowledges FWO for a "Krediet aan navorsers" 1.5.061.18N. NMRCoRe is supported by the Hercules Foundation (AKUL/13/21), by the Flemish Government as an international research infrastructure (I001321N), and by Department EWI via the Hermes Fund (AH.2016.134). The authors acknowledge FWO Vlaanderen and the teams at DUBBLE beamlines (ESRF, Grenoble) for financial and experimental support, respectively. Y.D.C. acknowledges the support from the Fund for Scientific Research-Flanders (FWO) (1234222N). S.V.C. thanks FWO Vlaanderen for financial support (12R8218N), and acknowledges KU Leuven for financing equipment required for harmonic light scattering (3E230460). A.D. acknowledges FWO Vlaanderen (G086522N) and KU Leuven (3E190382) for financial support.

7.References

1 S. M. Moosavi, A. Nandy, K. M. Jablonka, D. Ongari, J. P. Janet, P. G. Boyd, Y. Lee, B. Smit and H. J. Kulik, *Nat. Commun.*, 2020, **11**, 1–10.

2 M. Eddaoudi, D. B. Moler, H. Li, B. Chen, T. M. Reineke, M. O'Keeffe and O. M. Yaghi, *Acc. Chem. Res.*, 2001, **34**, 319–330.

3 M. J. Van Vleet, T. Weng, X. Li and J. R. Schmidt, *Chem. Rev.*, 2018, **118**, 3681–3721.

4 B. Jin, S. Wang, D. Boglaienko, Z. Zhang, Q. Zhao, X. Ma, X. Zhang and J. J. De Yoreo, *J. Cryst. Growth*, 2023, **603**, 126989.

5 J. Cravillon, S. Münzer, S. J. Lohmeier, A. Feldhoff, K. Huber and M. Wiebcke, *Chem. Mater.*, 2009, **21**, 1410–1412.

6 M. P. Attfield and P. Cubillas, *Dalt. Trans.*, 2012, **41**, 3869–3878.

7 C. Jamieson, E. M. Moir, Z. Rankovic and G. Wishart, *J. Med. Chem.*, 2006, **49**, 12–14.

8 G. Férey, M. Haouas, T. Loiseau and F. Taulelle, *Chem. Mater.*, 2014, **26**, 299–309.

9 J. A. Allegretto, D. Onna, S. A. Bilmes and O. Azzaroni, .

10 R. Jain, A. J. Mallette and J. D. Rimer, *J. Am. Chem. Soc.*, 2021, **143**, 21446–21460.

11 M. Kumar, R. Li and J. D. Rimer, *Chem. Mater.*, 2016, **28**, 1714–1727.

12 X. Liu, S. W. Chee, S. Raj, M. Sawczyk, P. Král and U. Mirsaidov, *Proc. Natl. Acad. Sci. U. S. A.*, 2021, **118**, 1–7.

13 I. H. Lim, W. Schrader and F. Schüth, *Chem. Mater.*, 2015, **27**, 3088–3095.

14 A. Deacon, L. Briquet, M. Malankowska, F. Massingberd-Mundy, S. Rudi, T. Hyde, H. Cavaye, J. Coronas, S. Poulston and T. Johnson, *Commun. Chem.*, 2022, **5**, 1–10.

15 J. Cravillon, C. A. Schröder, R. Nayuk, J. Gummel, K. Huber and M. Wiebcke, *Angew. Chem. Int. Ed. Engl.*, 2011, **50**, 8067–71.

16 J. Cravillon, C. A. Schröder, R. Nayuk, J. Gummel, K. Huber and M. Wiebcke, *Angew. Chemie - Int. Ed.*, 2011, **50**, 8067–8071.

17 J. Cravillon, C. A. Schröder, H. Bux, A. Rothkirch, J. Caro and M. Wiebcke, *CrystEngComm*, 2012, **14**, 492–498.

18 M. W. Terban, D. Banerjee, S. Ghose, B. Medasani, A. Shukla, B. A. Legg, Y. Zhou, Z. Zhu, M. L. Sushko, J. J. De Yoreo, J. Liu, P. K. Thallapally and S. J. L. Billinge, *Nanoscale*, 2018, **10**, 4291–4300.

19 J. P. Patterson, P. Abellan, M. S. Denny, C. Park, N. D. Browning, S. M. Cohen, J. E. Evans and N. C. Gianneschi, *J. Am. Chem. Soc.*, 2015, **137**, 7322–7328.

20 F. Carraro, J. D. Williams, M. Linares-Moreau, C. Parise, W. Liang, H. Amenitsch, C. Doonan, C. O. Kappe and P. Falcaro, *Angew. Chemie*, 2020, **132**, 8200–8204.

21 E. L. Bustamante, J. L. Fernández and J. M. Zamaro, *J. Colloid Interface Sci.*, 2014, **424**, 37–43.

22 X. Wu, H. Yue, Y. Zhang, X. Gao, X. Li, L. Wang, Y. Cao, M. Hou, H. An, L. Zhang, S. Li, J. Ma, H. Lin, Y. Fu, H. Gu, W. Lou, W. Wei, R. N. Zare and J. Ge, *Nat. Commun.*, 2019, **10**, 1–8.

23 Y. Zhu, J. Ciston, B. Zheng, X. Miao, C. Czarnik, Y. Pan and R. Sougrat, 2017, **16**, 4–9.

24 A. F. Ogata, A. M. Rakowski, B. P. Carpenter, D. A. Fishman, J. G. Merham, P. J. Hurst and J. P. Patterson, *J. Am. Chem. Soc.*, 2020, **142**, 1433–1442.

25 J. D. Rimer and M. Tsapatsis, *MRS Bull.*, 2016, **41**, 393–398.

26 K. N. Olafson, R. Li, B. G. Alamani and J. D. Rimer, *Chem. Mater.*, 2016, **28**, 8453–8465.

27 J. D. Rimer, A. Chawla and T. T. Le, *Annu. Rev. Chem. Biomol. Eng.*, 2018, **9**, 283–309.

28 M. Filez, C. Caratelli, M. Rivera-torrente, A. J. R. Heck, V. Van, M. Bert, M. Filez, C. Caratelli, M. Rivera-torrente, F. Muniz-miranda, M. Hoek, M. Altelaar, A. J. R. Heck, V. Van Speybroeck and B. M. Weckhuysen, *Cell Reports Phys. Sci.*, 2021, **2**, 100680.

29 Z. Öztürk, M. Filez and B. M. Weckhuysen, *Chem. - A Eur. J.*, 2017, **23**, 10915–10924.

30 S. R. G. Balestra, B. Martínez-Haya, N. Cruz-Hernández, D. W. Lewis, S. M. Woodley, R. Semino, G. Maurin, A. R. Ruiz-Salvador and S. Hamad, *Nanoscale*, 2023, **15**, 3504–3519.

31 H. H. M. Yeung, A. F. Sapnik, F. Massingberd-Mundy, M. W. Gaultois, Y. Wu, D. A. X. Fraser, S. Henke, R. Pallach, N. Heidenreich, O. V. Magdysyuk, N. T. Vo and A. L. Goodwin, *Angew. Chemie - Int. Ed.*, 2019, **58**, 566–571.

32 S. Van Cleuvenbergen, Z. J. Smith, O. Deschaume, C. Bartic, S. Wachsmann-Hogiu, T. Verbiest and M. A. van der Veen, *Nat. Commun.*, 2018, **9**, 1–9.

33 S. Van Cleuvenbergen, I. Stassen, E. Gobechiya, Y. Zhang, K. Markey, D. E. De Vos, C. Kirschhock, B. Champagne, T. Verbiest and M. A. Van Der Veen, *Chem. Mater.*, 2016, **28**, 3203–3209.

34 K. Markey, T. Putzeys, P. Horcajada, T. Devic, N. Guillou, M. Wübbenhorst, S. Van Cleuvenbergen, T. Verbiest, D. E. De Vos and M. A. Van Der Veen, *Dalt. Trans.*, 2016, **45**, 4401–4406.

35 A. R. Dok, T. Legat, Y. de Coene, M. A. van der Veen, T. Verbiest and S. Van Cleuvenbergen, *J. Mater. Chem. C*, 2021, **9**, 11553–11568.

36 Y. De Coene, O. Deschaume, S. Jooken, S. Seré, S. Van Cleuvenbergen, C. Bartic, T. Verbiest

and K. Clays, *Chem. Mater.*, 2020, **32**, 7327–7337.

37 M. Moris, M. P. Van Den Eede, G. Koeckelberghs, O. Deschaume, C. Bartic, S. Van Cleuvenbergen, K. Clays and T. Verbiest, *Commun. Chem.*, 2019, **2**, 1–9.

38 M. Moris, M. P. Van Den Eede, G. Koeckelberghs, O. Deschaume, C. Bartic, K. Clays, S. Van Cleuvenbergen and T. Verbiest, *Macromolecules*, 2020, **53**, 9513–9520.

39 M. Moris, M. P. Van Den Eede, G. Koeckelberghs, O. Deschaume, C. Bartic, K. Clays, S. Van Cleuvenbergen and T. Verbiest, *Macromolecules*, 2021, **54**, 2477–2484.

40 K. Aerts, O. Deschaume, C. Bartic, S. van Cleuvenbergen, K. Clays, G. Koeckelberghs, T. Verbiest and Y. de Coene, *Macromolecules*, 2024, **57**, 1521–1531.

41 N. Van Steerteghem, K. Clays, T. Verbiest and S. Van Cleuvenbergen, *Anal. Chem.*, 2017, **89**, 2964–2971.

42 V. R. Thierry Verbiest, Koen Clays, *Second-order Nonlinear Optical Characterization Techniques le*, CRC Press, 2009.

43 K. D. M. Harris, C. E. Hughes, P. A. Williams and R. Gregory, 2017, 137–148.

44 C. E. Hughes, P. A. Williams, B. M. Kariuki and K. D. M. Harris, 2018, 1–6.

45 N. Pellens, N. Doppelhammer, S. Radhakrishnan, K. Asselman, C. V. Chandran, D. Vandenabeele, B. Jakoby, J. A. Martens, F. Taulelle, E. K. Reichel, E. Breynaert and C. E. A. Kirschhock, *Chem. Mater.*, 2022, **34**, 7139–7149.

46 F. Wang, V. N. Richards, S. P. Shields and W. E. Buhro, *Chem. Mater.*, 2014, **26**, 5–21.

47 H. H. -M. Yeung, A. F. Sapnik, F. Massingberd-Mundy, M. W. Gaultois, Y. Wu, D. A. X. Fraser, S. Henke, R. Pallach, N. Heidenreich, O. V. Magdysyuk, N. T. Vo and A. L. Goodwin, *Angew. Chemie - Int. Ed.*, 2019, **58**, 566–571.

48 A. F. Möslein, L. Donà, B. Civalleri and J.-C. Tan, *Defects in ZIF-8 crystallization and their impact on mechanical properties*, .

49 M. Houlleberghs, A. Hoffmann, D. Dom, C. E. A. Kirschhock, F. Taulelle, J. A. Martens and E. Breynaert, *Anal. Chem.*, 2017, **89**, 6940–6943.

50 H. Vanderschaeghe, M. Houlleberghs, L. Verheyden, D. Dom, C. V. Chandran, S. Radhakrishnan, J. A. Martens and E. Breynaert, *Anal. Chem.*, 2023, **95**, 1880–1887.

51 C. Grunewald, R. Seidel and A. Chapartegui-arias, 2020, 8–11.

52 S. Saha, S. Springer, M. E. Schweinefuß, D. Pontoni, M. Wiebcke and K. Huber, *Cryst. Growth Des.*, 2016, **16**, 2002–2010.

53 S. R. Venna, J. B. Jasinski and M. A. Carreon, *J. Am. Chem. Soc.*, 2010, **132**, 18030–18033.

54 G. D. Van Driessche, Alexander E.S., Kellermeier Matthias , Benning Liane G., *New Perspectives on Mineral Nucleation and Growth From Solution Precursors to Solid Materials*, Springer Berlin Heidelberg, 2017.

55 J. De Yoreo, *Cryst. via Nonclassical Pathways Vol. 1 Nucleation, Assem. Obs. Appl. Part 1 - A Perspect. Multistep Pathways Nucleation*, 2020, **1**, 1–17.

56 X. Zhang, ed. X. Zhang, American Chemical Society, 1358th edn., 2020.

57 L. Priandani, A. Aliefa, O. P. Arjasa and F. I. Pambudi, *Bull. Chem. React. Eng. Catal.*, 2023, **18**,

521–538.

58 J. Cravillon, R. Nayuk, S. Springer, A. Feldhoff, K. Huber and M. Wiebcke, *Chem. Mater.*, 2011, **23**, 2130–2141.

59 Y. De Coene, S. Van Cleuvenbergen, N. Van Steerteghem, V. Baekelandt, T. Verbiest, C. Bartic and K. Clays, *J. Phys. Chem. C*, 2017, **121**, 6909–6915.